Supporting information

Boosting oxygen redox reversibility in chemo-mechanically robust Li-rich oxides cathode *via* multi-scale defect design

Fangkun Li[1], Yenchen Lin[1], Junhao Liu[1], Jiahe Chen[1], Xuanhong Wan[1], Linwei Zhao[1], Lei Xi[1], Zheng Li[2], Hangyu Zhang[2], Xijun Xu[2], Zhidu Zhou[3], Baitao Su[3], Min Zhu[1], Jun Liu[1,*]

[1]Guangdong Provincial Key Laboratory of Advanced Energy Storage Materials, School of Materials Science and Engineering, South China University of Technology, Guangzhou 510641, China

[2]Group of Organic Optoelectronic Materials and Functional Macromolecules, School of Chemical Engineering and Light Industry, Guangdong University of Technology, Guangzhou 510006, China

[3]Jiangmen Kanhoo Industry Co., Ltd., Jiangmen 529040, China

[*]Corresponding authors: msjliu@scut.edu.cn

Experimental section

Materials Synthesis

In a typical process[1,2], based on the atomic molar ratios in $Li_{1.2}Ni_{0.13}Co_{0.13}Mn_{0.54}O_2$, 1.636 g of $(CH_3COO)_2Mn{\cdot}4H_2O$, 0.416 g of $(CH_3COO)_2Ni{\cdot}4H_2O$, 0.416 g of $(CH_3COO)_2Co{\cdot}4H_2O$, and 1.608 g of $CH_3COOLi{\cdot}2H_2O$ were dissolved in 240 ml of a binary ethanol-water solvent mixture (ethanol: water volume ratio = 5:1, the same below) under stirring. On the other hand, 1.628 g of $H_2C_2O_4$ was dissolved in 120 ml of ethanol-water mixed solution. The $H_2C_2O_4$ mixed solution was quickly infused into the metal acetate mixed solution under stirring for 6 h (The determination of the reaction time is detailed in Fig. S1, 2). The $MC_2O_4{\cdot}xH_2O$ (*M*=Li, Ni, Co and Mn) precursor was collected by evaporating ethanol/water from the solvent mixture in air drying at 80 °C for 24 h. The as-prepared $MC_2O_4{\cdot}xH_2O$ precursor was sintered at 300 °C for 2 h, next at 480 °C for 8 h and then at 800 °C for 15 h in air with a heating rate of 2.0 °C min^{-1} to obtain the final 1D micro/nanostructured $Li_{1.2}Ni_{0.13}Co_{0.13}Mn_{0.54}O_2$ (named Li2-LROs) material. Lithium-deficient $Li_{1.2}Ni_{0.13}Co_{0.13}Mn_{0.54}O_2$ (named S-LROs) materials have been prepared. The solvent, oxalate precipitates, and reaction residual solutes in the mixed solution were separated by filtration, and the lithium-deficient $MC_2O_4{\cdot}xH_2O$ precursor was obtained by drying the precipitates at 80 °C for 24 h. The lithium-deficient precursor was subjected to the same sintering process to obtain S-LROs. As a comparison, $Li_{1.1}Ni_{0.13}Co_{0.13}Mn_{0.54}O_2$ (named Li1-LROs) materials were synthesized using the same method as for the preparation of Li2-LROs.

Materials Characterizations

The X-ray diffraction (XRD) measurements were employed using a PANalytical Empyrean X-ray diffraction with Cu-K_α radiation source λ = 1.5046 Å at a scan increment of 0.013°, in the 2θ range of 10–120°. *In-situ* XRD was carried out using a specially designed cell with a Be window, which was cycled with the current density of 0.2 C and the 2θ scan range of 15–73°. The data collected was fitted by Rietveld refinement (GSAS/EXPGUI software). Scanning electron microscope (SEM) and time of flight secondary ion mass spectrometry (TOF-SIMS) were characterized on a TESCAN GAIA3. High-resolution transmission electron microscope (HRTEM)

images were performed on a FEI Talos F200x. Geometric phase analysis (GPA) measurements were executed by means of an in-house developed software titled Strain++[3]. Nitrogen adsorption/desorption isotherms at 77 K were determined using a Quadrachrome Adsorption Instrument. X-ray photoelectron spectroscopy (XPS) was performed to determine the distribution of each element using ThermoFisher ESCALAB Xi+ with Al K_α radiation. The X-ray absorption near-edge spectra (XANES) and extended X-ray absorption fine structure (EXAFS) of Ni/Mn *K*-edge spectra were collected by easyXAFS300$^+$. The electron paramagnetic resonance (EPR) spectra were conducted with a CIQTEK EPR200-plus. Raman spectra were detected on a Renishaw in via Queue/Reflex (λ = 532 nm). Thermal Gravimetric (TG) data were obtained using a Q50 thermogravimetric analyzer. Differential scanning calorimetry (DSC) analysis was performed between 50 °C and 450 °C by a DSC TA-Q20 System at a heating rate of 10 °C min^{-1}. Inductively coupled plasma optical emission spectrometry (ICP-OES) was obtained using iCAP 7200 Duo. The concentrations of Ni/Co/Mn element dissolved on the Li-metal anode after a long cycling were collected using an inductively coupled plasma mass (ICP-MS, iCAP RQ). Nanoindentations were detected on the fresh electrodes or after 50 cycles using Anton Paar triboindenter (STEP 700) with berkovich diamond indenter (Serial number: BBI-36, α= 65.3°± 0.3°). Indentations with a maximum load of 5 mN were conducted by loading, holding and uploading for 10 s, 5 s and 10 s, respectively. The cycled cells were disassembled in an Ar atmosphere glove box and the electrodes were cleaned with dimethyl carbonate (DEC) and collected for further failure mechanism characterization. Magnetic field imaging (MFI) analysis was performed on a B-Lab 160S. Fluke RSE30/60 *online* infrared thermal imaging cameras were used to collect thermal imaging information from the pouch-type half cells.

Electrochemical Measurements

The working cathode electrodes were consisted of 80 wt% active materials, 10 wt% super-P, and 10 wt% polyvinylidene fluoride binder (PVDF) binder in N-methyl-2-pyrrolidone (NMP) solvent. The obtained slurry was casted on an Al foil with a mass loading of 2.5± 0.3 mg cm^{-2} and dried at 110 °C in a vacuum oven overnight. 1 M

$LiPF_6$ dissolved in ethylene carbonate/ dimethyl carbonate/ethyl methyl carbonate (EC/DEC/EMC, 3:2:5 by vol%) was used as an electrolyte. Li foil or Si-C was used as the anode and Celgard 2325 was used as the separator. The Si-C anode electrodes were consisted of 80 wt% active materials, 10 wt% super-P, 2 wt% carboxymethyl cellulose (CMC), 3 wt% styrene-butadiene rubber (SBR) and 5 wt% poly(acrylic acid) (PAA) in deionized water solvent. The slurries were uniformly coated on a Cu foil and dried in a vacuum at 80 °C for 12 h. The Negative/Positive (N/P) ratio is about 1.2 for the S-LROs/Si-C full cell. All cells (including coin-type, pouch and specially designed cells) were assembled in an argon-filled glove box (H_2O, $O_2 \leq$ 0.1 ppm). Galvanostatic charge–discharge test was conducted on a LAND battery testing system (CT3001A) in the potential range of 2.0–4.8 V (*vs* Li/Li^+). The cyclic voltammetry (CV) and electrochemical impedance spectroscopy (EIS) measurements were tested using a Gamry electrochemical workstation (Interface 1000E). The *in-situ* EIS was conducted on Interface 1000E or 5000E, Biologic under the current density of 0.1 C at 30 ℃, and the frequency range is from 10^6 Hz to 10^{-2} Hz with a perturbation of 5 mV. The distribution of relaxation time (DRT) analysis was processed by the MATLAB Graphical user DRTtools that was developed by Ciucci's research team[4]. The galvanostatic intermittent titration technique (GITT) was performed with a 10 min charge/discharge at 0.1 C followed by 60 min of relaxation.

Fig. S1 Color of the solution as a function of mixed reaction time

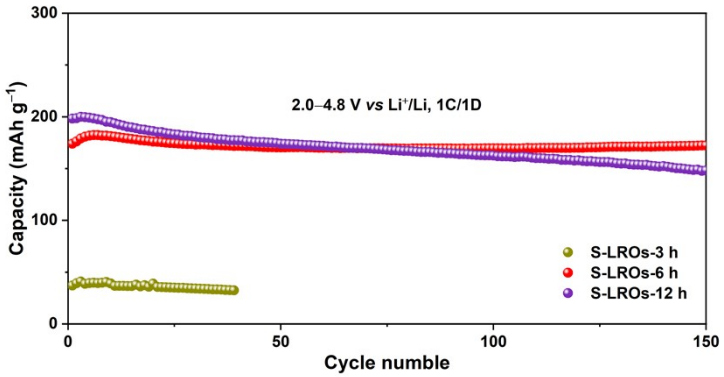

Fig. S2 The cycling performance of the samples prepared by filtration after different reaction times of the mixed solutions. S-LROs-3, S-LROs-6 and S-LROs-12 denote solution reaction times of 3 h, 6 h and 12 h, respectively. The sintering process was the same as that for the preparation of Li2-LROs.

As demonstrated in Fig. S1 the color of the solution gradually changed to white as the reaction time increased. In particular, the solution was white at 6 h and did not change significantly in subsequent reactions. Electrochemical stability tests were performed on the samples prepared with different reaction times and the results are shown in Fig. S2. S-LROs-3 has a relatively low capacity of the prepared material due to the insufficient reaction (3 h). S-LROs-12 has a longer reaction time and precipitates more lithium, which exhibits a higher initial discharge specific capacity. Unfortunately, the cycling stability of S-LROs-12 is poorer compared to the sample synthesized with 6 h of reaction (S-LROs-6). Therefore, the main study was carried out on S-LROs-6, labeled as S-LROs.

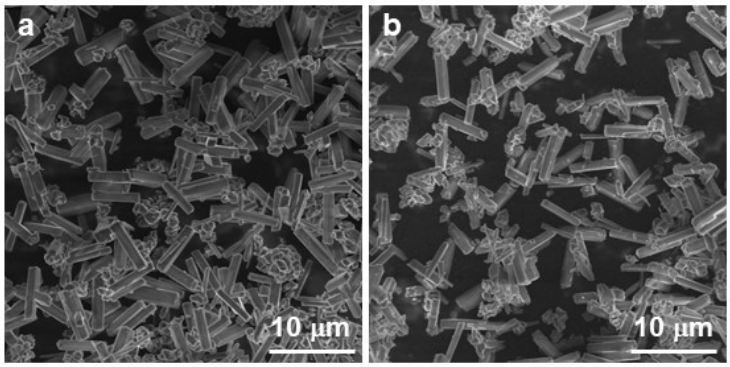

Fig. S3 SEM images of $MC_2O_4 \cdot xH_2O$ (M= Li, Ni, Co and Mn) precursor for Li2-LROs (a) and S-LROs (b).

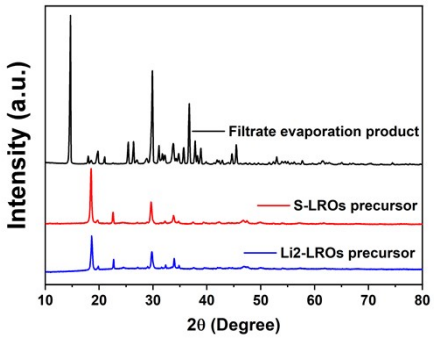

Fig. S4 XRD pattern of filtrate evaporation product (black) and $MC_2O_4 \cdot xH_2O$ (M= Li, Ni, Co and Mn) precursor for Li2-LROs (blue) and S-LROs (red).

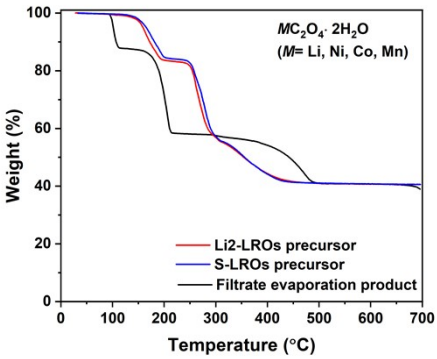

Fig. S5 TG curve of filtrate evaporation product (black) and $MC_2O_4 \cdot xH_2O$ (M= Li, Ni, Co and Mn) precursor for Li2-LROs (blue) and S-LROs (red).

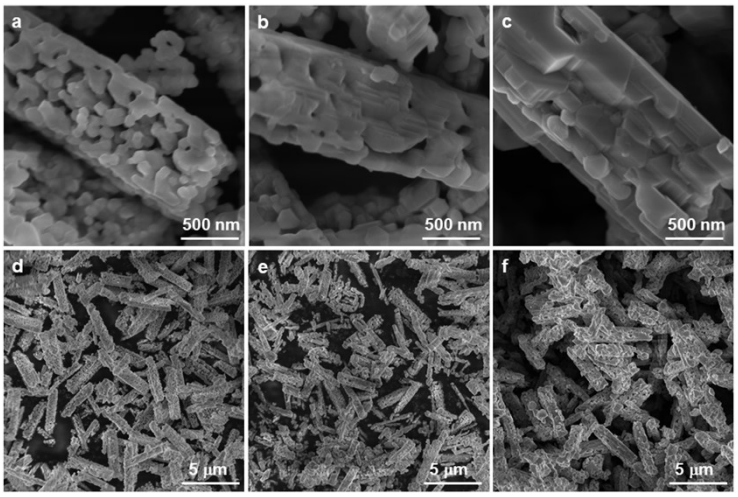

Fig. S6 SEM images of the Li2-LROs (a, d), Li1-LROs (b, e) and S-LROs (c, f). As far as morphology is concerned Li1-LROs and S-LROs material particles are more closely aligned than Li2-LROs. This suggests that lithium deficiency engineering can induce the formation of larger and densely arranged primary particles in the material.

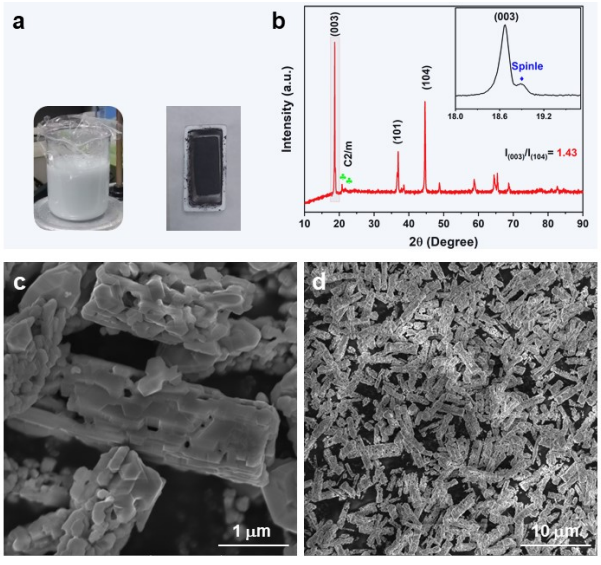

Fig. S7 Reproducible experiments for S-LROs material preparation (marked as Re-S-LROs). (a) Optical photographs of the reaction solution (left), and sintered product (right) for Re-S-LROs. XRD pattern (Insets is the enlarged patterns) (b) and SEM images (c, d) of Re-S-LROs. The re-prepared S-LROs were characterized by the detection of spinel in XRD pattern and the observation of larger and tightly aligned primary particles in SEM images. It indicates that the synthetic method for preparing multiscale defective LROs by filtration is reproducible.

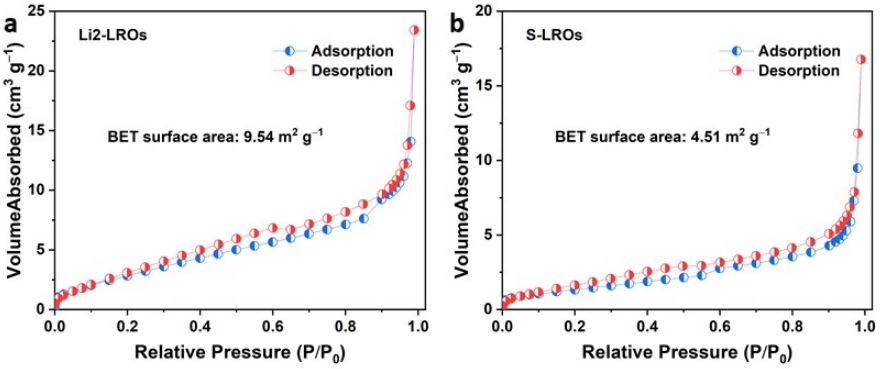

Fig. S8 The N_2 adsorption/desorption isotherms for (a) Li2-LROs and (b) S-LROs.

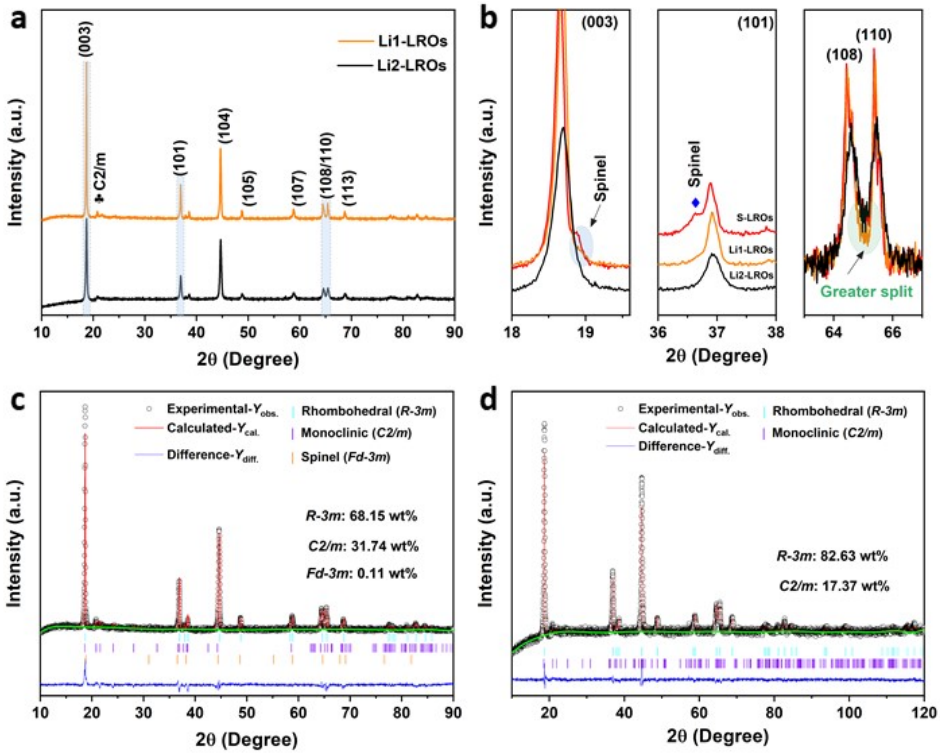

Fig. S9 XRD patterns (a) and (003), (101) and (108)/(110) peaks enlarged patterns (b) of Li1-LROs and Li2-LROs, respectively. Rietveld Refinement of XRD pattern for Li1-LROs (c) and Li2-LROs (d).

As shown in Fig. S9a, the Li1-LROs have a typical α-$NaFeO_2$ layered structure and a honeycomb-ordered structure of monoclinic Li_2MnO_3. In addition, a weak spinel phase diffraction peak was also observed at ~18.88° (Fig. S9b). The refinement results show that its spinel content is minimal (Fig. S9c and Table S1). However, the C2/m phase of 31.74% for Li1-LROs was higher than that of 17.37% for Li2-LROs. Li1-LROs is more

split than the (108/110) peaks of Li2-LROs and S-LROs (Fig. S9b), indicating that Li1-LROs possess a more highly ordered structure[2]. Meanwhile, the I(003)/I(104) value of 1.81 for Li1-LROs was higher than that for other LROs (Table S1), demonstrating that Li1-LROs have less anionic mixing and exclusion.

Table S1. Rietveld Refined crystallographic parameters

Sample			Li2-LROs	Li1-LROs	S-LROs
Lattice Parameters	$R\bar{3}m$	a (Å)	2.851	2.851	2.854
		c (Å)	14.229	14.228	14.251
		c/a (Å)	4.991	4.991	4.993
		V (Å^3)	100.128	100.144	100.512
	C2/m	a (Å)	5.153	4.981	4.997
		b (Å)	8.102	8.534	8.564
		c (Å)	4.950	5.052	5.072
		V (Å^3)	204.146	202.464	204.020
	$Fd\bar{3}m$	a (Å)	/	8.156	8.228
Percentage compositions (wt.%)	$R\bar{3}m$ ($LiTMO_2$)		82.63	68.15	74.18
	C2/m (Li_2MnO_3)		17.37	31.74	23.26
	$Fd\bar{3}m$ ($Li_4Mn_5O_{12}$)		/	0.11	2.56
	Li/Ni cation mixing ($I_{(003)}/I_{(104)}$)		1.15	1.81	1.57
	wRp		1.83	2.46	2.44
	Rp		1.35	1.66	1.59
	χ^2		1.179	2.063	2.136

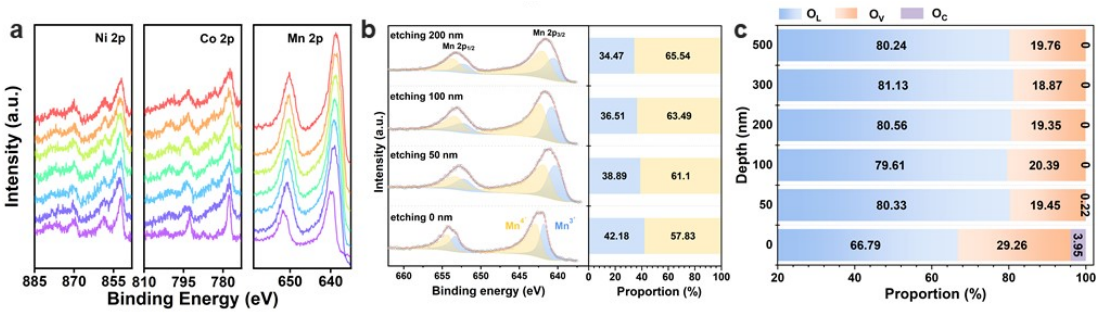

Fig. S10 (a) XPS spectra of Ni 2p, Co 2p, Mn 2p with different depths in the S-LROs. (b) XPS spectra of Mn 2p and the proportion of Mn^{3+} and Mn^{4+} ions at different etching depths of S-LROs. (c) The proportion of O_L, O_V and O_C at different etching depths of

S-LROs.

The in-depth XPS analysis in Fig. S10a demonstrates Ni, Co and Mn concentration uniformity, indicating that Ni/Co/Mn was distributed evenly from the surface of the S-LROs material to the bulk, in agreement with the EDS results (Fig. S11). Notably, there is more Mn^{3+} on the surface of S-LROs, which may be due to the introduction of O_V leading to charge equilibrium by reduction of Mn^{4+} (Fig. 10b). The percentage of O_V exhibits a notable decline (from 29.26% to 19.45%) with increasing etching depth, subsequently exhibiting a tendency to reach equilibrium (Fig. 10c). This trend is analogous to the observed enrichment of Mn^{3+} on the surface (Fig. 10b).

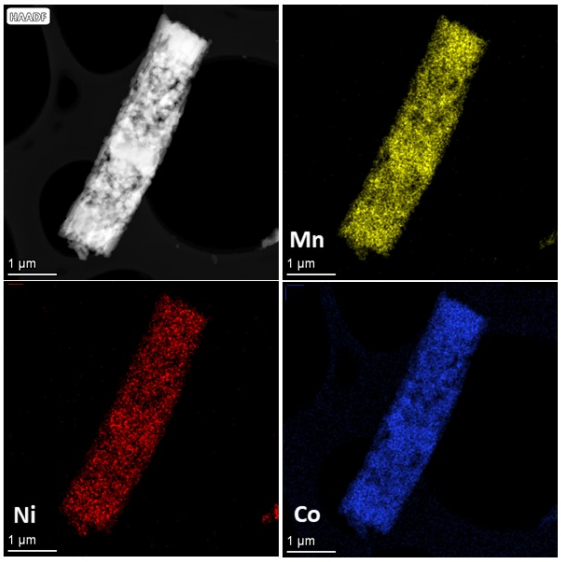

Fig. S11 EDS mapping of Mn, Ni and Co elements for S-LROs sample.

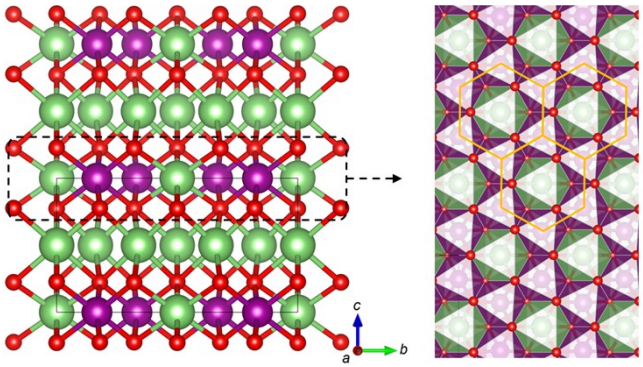

Fig. S12 Layered structure of Li_2MnO_3 with localized $Li@Mn_6$ superstructure units

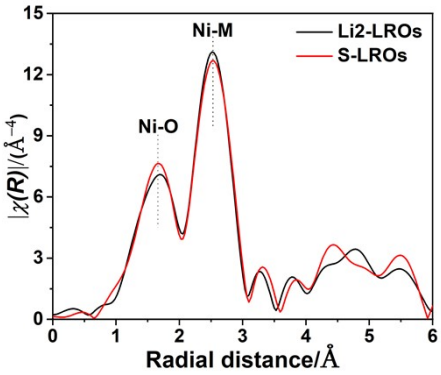

Fig. S13 EXAFS R space curves of Li2-LROs and S-LROs.

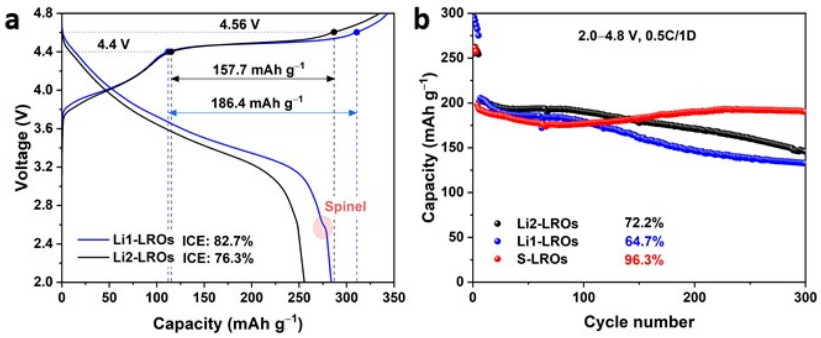

Fig. S14 (a) Initial charge/discharge curves of Li1-LROs and Li2-LROs. (b) Cycle performance of Li1-LROs, Li2-LROs and S-LROs at 1 C (0.5 C charge followed by 1 C discharge).

In order to exclude the effect of Li-deficient LROs materials obtained by evaporation of the solvent, $Li_{1.1}Ni_{0.13}Co_{0.13}Mn_{0.54}O_2$ cathode material (named Li1-LROs) was synthesized. Clearly, the discharge curves of the Li-poor Li1-LROs materials show a plateau associated with the spinel phase at around 2.6 V (Fig. S14a). The presence of spinel phase enhances the reversibility of the redox reaction, which leads to an increase in the initial Coulombic efficiency. In addition, S-LROs delivers a specific capacity of 186.4 mAh g^{-1} within the voltage range of 4.4~4.56 V, which was higher than that of Li2-LROs of 157.7 mAh g^{-1}, revealing a more boost activation of the Li_2MnO_3 phase in Li2-LROs. As the name implies, the discharge capacity of Li1-LROs is higher than that of Li2-LROs. As shown in Fig. S14b, the initial discharge specific capacity of 283.7 mAh g^{-1} for Li1-LROs, which is higher than that of other LROs. From the structural point of view, the X RD refinement results are listed in Tables S1. On the one hand, it may be attributed to the lower degree of anion mixing and more structural

ordering of Li1-LROs. On the other hand, it is attributed to the fact that it contains more Li_2MnO_3[5]. Unfortunately, the excess Li_2MnO_3 also causes Li1-LROs to exhibit poor cycling stability. It requires a trade-off in terms of high specific capacity and cycling stability. As expected, exhibited in Fig. S14b, the S-LROs delivered a higher capacity and enhanced cyclability (190.6 mAh g^{-1} and 96.3%, respectively) after 300 cycles than that of Li1-LROs (132.8 mAh g^{-1}, 64.7%) and Li2-LROs (146.0 mAh g^{-1}, 72.2%) during 0.5 C charging and 1 C discharging process. In addition, Capacity increases were observed during cycling for all LROs samples. The slight capacity increase demonstrates the presence of a slow but continuous activation process during cycling[6,7]. The activation rate may not be able to keep up with the capacity decay rate in the early stage because of the influence of the formation of the lithium metal solid electrolyte interphase (SEI) and the cathode electrolyte interphase (CEI) film. After the interface membrane (SEI/CEI) is stabilized in the later stage, the capacity decay rate is smaller than the activation rate. Ultimately, it shows the phenomenon of capacity decreasing first and then increasing.

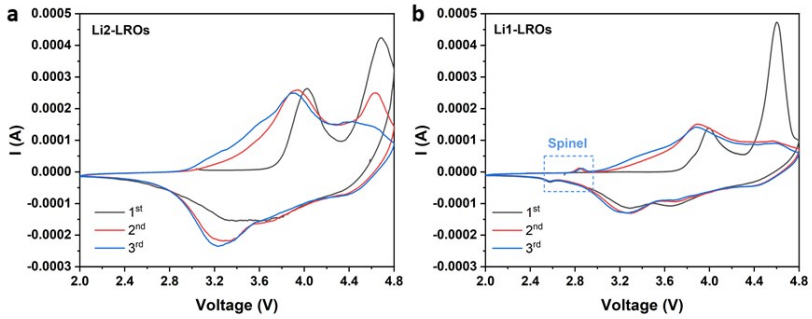

Fig. S15 CV curve of Li2-LROs (a) and Li1-LROs (b) at a scan rate of 0.1 mV s^{-1}.

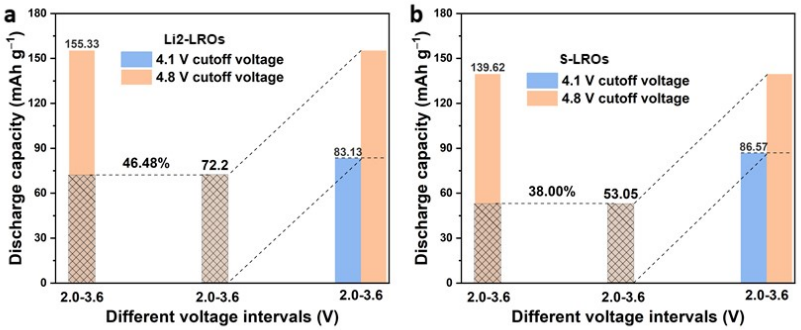

Fig. S16 The discharge capacity of Li2-LROs (a) and S-LROs (b) within different voltage ranges.

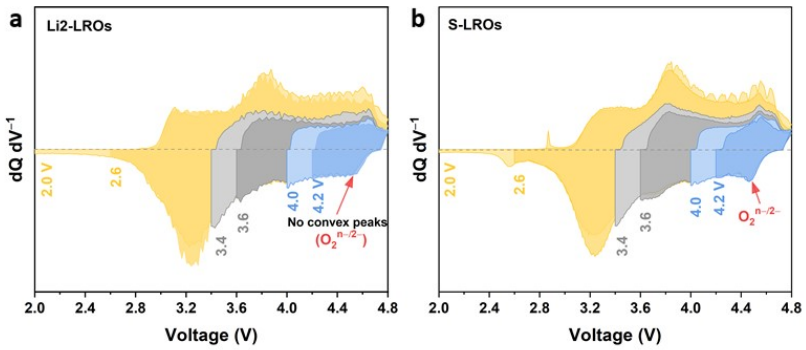

Fig. S17 The dQ dV^{-1} curves of Li2-LROs (a) and S-LROs (b) as the discharge window is opened stepwise from 4.8 to 2.0 V.

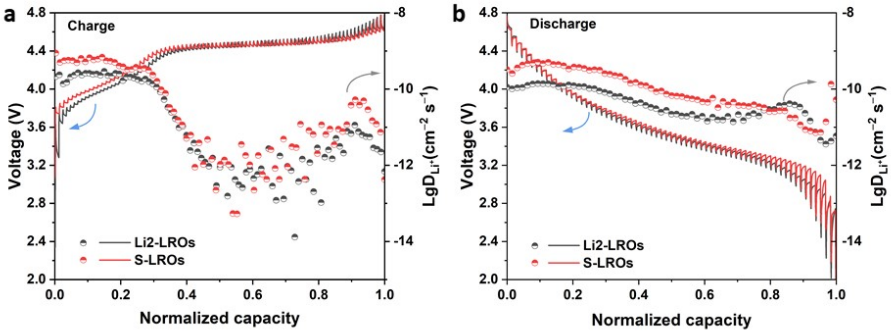

Fig. S18 The GITT measurements in the first cycle and the corresponding D_{Li^+} for charge/discharge process.

D_{Li^+} was derived by the galvanostatic intermittent titration technique (GITT) using the following equation. The equation is based on Fick's second law of diffusion and is simplified due to the quasi-linear relationship between the voltage ΔE_τ during the current pulse and the square root of the current pulse time $\sqrt{\tau}$[8].

$$D_{Li^+} = \frac{4}{\pi\tau}\left(\frac{n_M V_M}{S}\right)^2\left(\frac{\Delta E_S}{\Delta E_\tau}\right)^2$$

Here, τ represents the duration of the current pulse. n_M denotes the number of moles, while V_M is the molar volume of the electrode. S stands for the electrode-electrolyte contact area. ΔE_s and ΔE_τ are respectively the change in the steady-state potential and the total change during the current flux after deducting the IR drop.

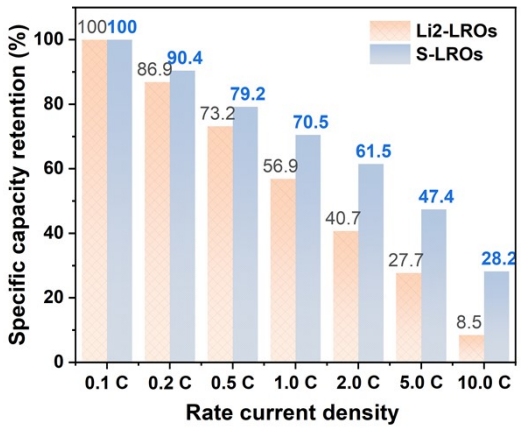

Fig. S19 Rate performance of Li2-LROs and S-LROs. The reversible retention results of different multiplicity discharge specific capacities relative to the 0.1 C rate discharge specific capacity indicate that S-LROs materials possess superior rate performance than Li2-LROs.

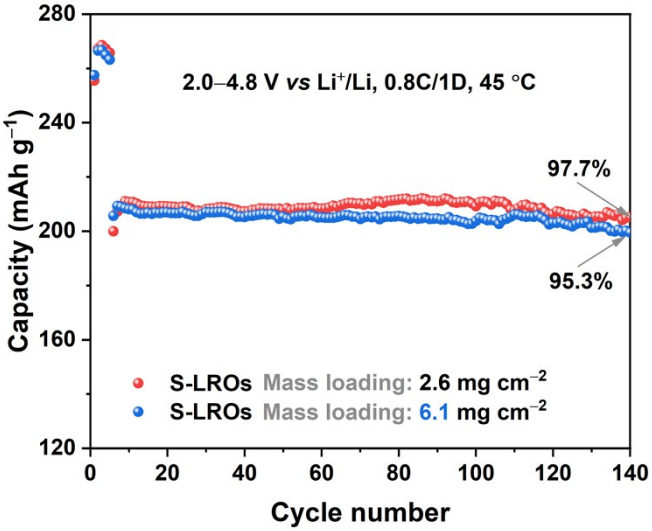

Fig. S20 Long-term cycling performance of S-LRO materials at 45 °C with different loadings. S-LROs still exhibited relatively excellent high-temperature cycling stability under higher loading conditions.

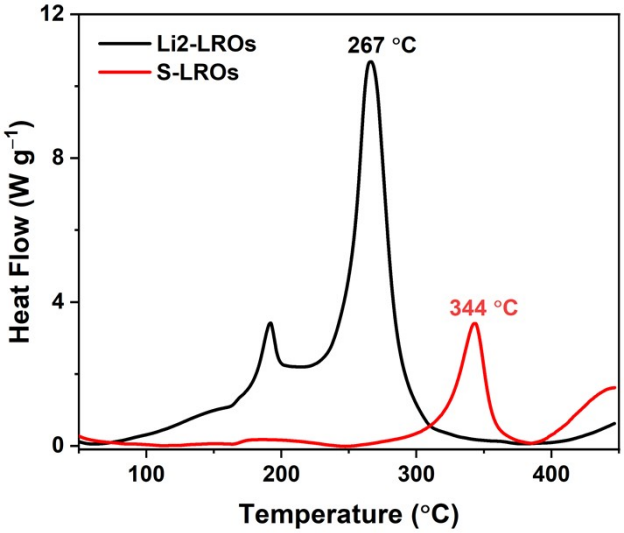

Fig. S21 DSC curves of Li2-LROs and S-LROs after charging at 4.8 V. As shown in Fig. S21, the second peak exothermic temperature of Li2-LROs electrodes is 267 °C, and the peak exothermic temperature of S-LROs electrodes is 344 °C, which indicates a better lattice oxygen stability as well as improved safety performance.

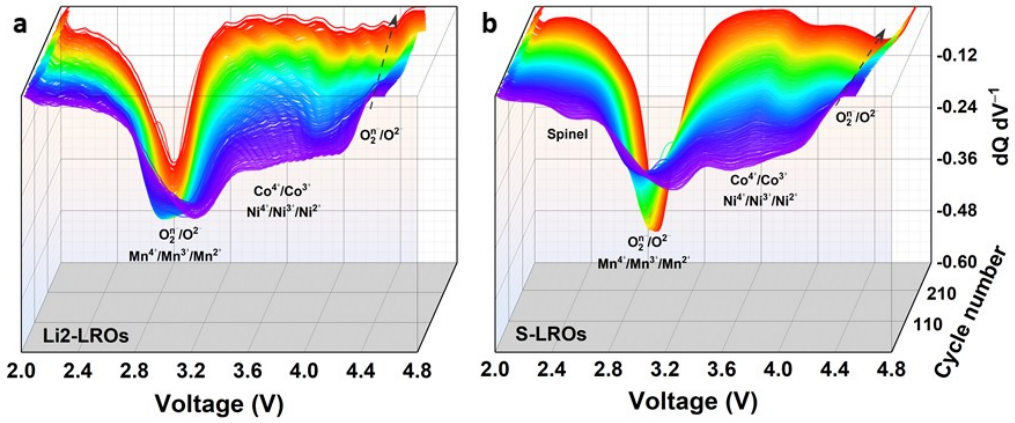

Fig. S22 The dQ dV^{-1} profiles of (a) Li2-LROs and (b) S-LROs with different cycles at 1 C.

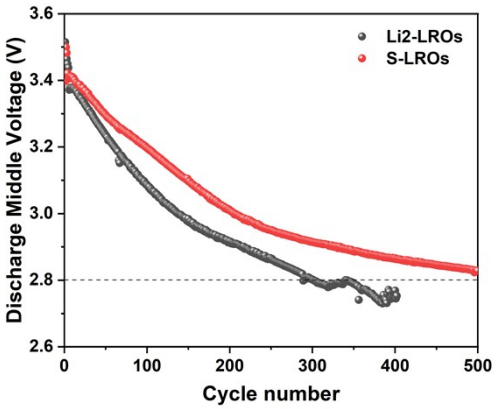

Fig. S23 The discharge middle voltage of Li2-LROs and S-LROs at 1 C and 30 °C.

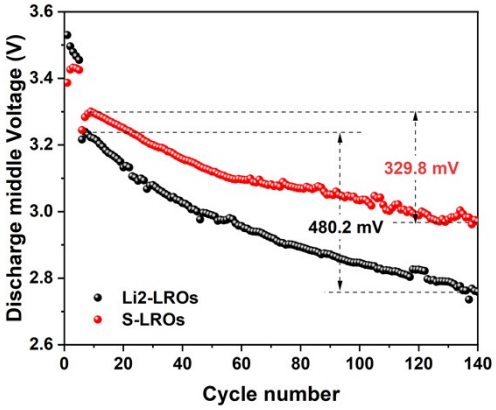

Fig. S24 The discharge middle voltage of Li2-LROs and S-LROs at 1 C and 45 °C.

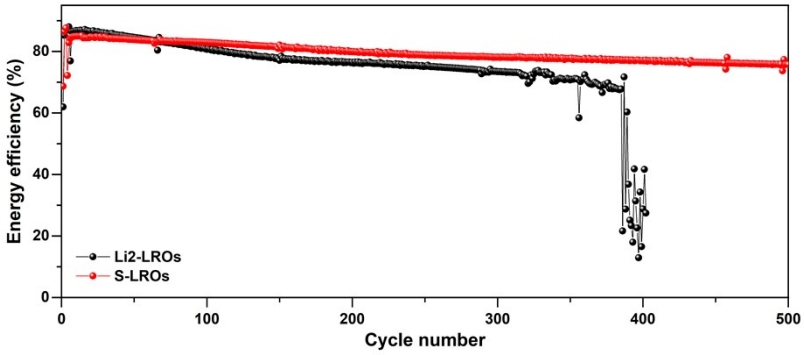

Fig. S25 The energy conversion efficiency curves of Li2-LROs and S-LROs during cycling.

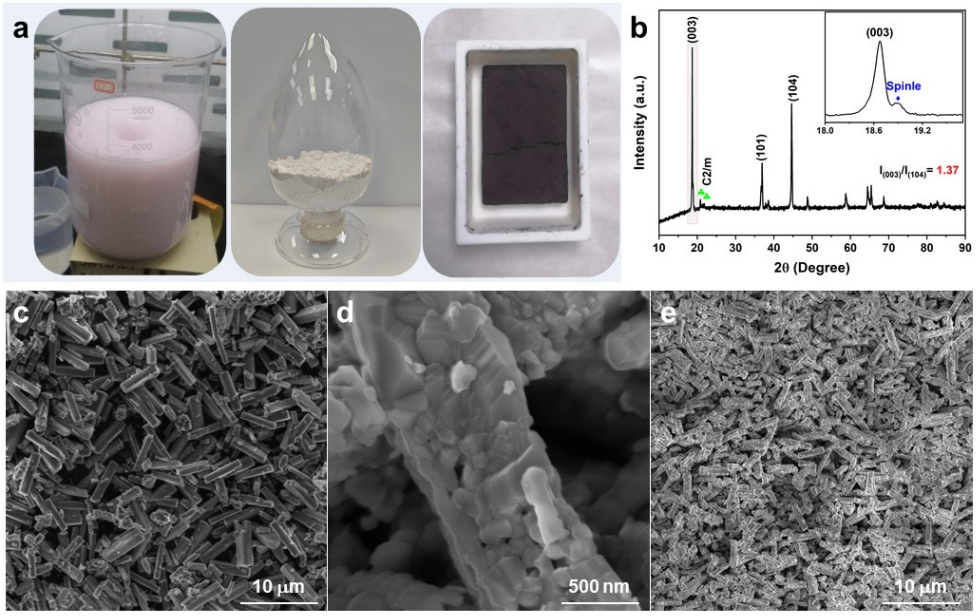

Fig. S26 Structural characterization of S-LROs material preparation scaled up 10- times (labeled as S-LROs-10x). (a) Optical photographs of the reaction solution (left), $MC_2O_4 \cdot xH_2O$ (*M*= Li, Ni, Co and Mn) precursor (center) and sintered product (right) for S-LROs-10x. (c) SEM image of $MC_2O_4 \cdot xH_2O$ precursor for S-LROs-10x. XRD pattern (Insets are the enlarged patterns) (b) and SEM images (d, e) of S-LROs-10x.

The S-LROs-10x material was synthesized by scaling up the raw materials for the preparation of S-LROs in the same proportion by a factor of 10 (Fig. S26a). As depicted in the Fig. S26c, the morphology of the $MC_2O_4 \cdot xH_2O$ (*M*= Li, Ni, Co and Mn) precursor obtained from the scaled-up preparation remained a micro-nano rod-like structure and was not significantly damaged after sintering (Fig. S26d). The primary particles of the rod-like structure are similar to those of S-LRO, which are large and compact (Fig. S26d). Fig. S26b depicts the typical XRD pattern of the S-LROs-10x. All of the diffraction peaks can be indexed to the α-$NaFeO_2$ type layered structure (space group: R $\bar{3}$m) with additional weak short-ranged superlattice reflections around 2θ= 20-25°, corresponding to the ordering of Li and Mn atoms in the transition metal layers of Li_2MnO_3 component with space group C/2m. Obviously, analogous to S-LROs, the $Li_4Mn_5O_{12}$ spinel phase was detected in the XRD of S-LROs-10x (Fig. S26b, insets). More importantly, a plateau associated with the spinel phase is similarly observed in the discharge curve around 2.6 V (Fig. S27). In addition, S-LROs-10x exhibits an upper

initial Coulomb efficiency of 86.4% comparable to that of S-LROs, which is higher than that of Li2-LROs and Li1-LROs. The results reveal that the structural and electrochemical characterization of the S-LROs material is reproducible in scaled-up preparations.

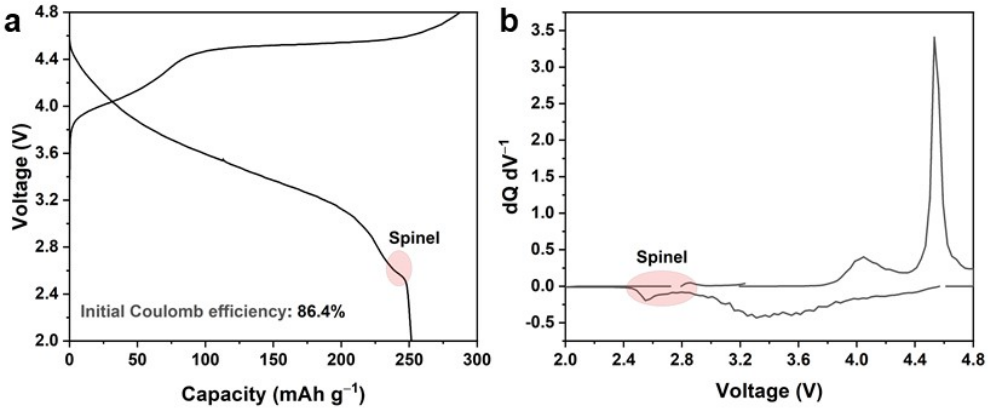

Fig. S27 The initial charge/discharge (a) and corresponding dQ dV^{-1} (b) curves in the voltage range 2.0–4.8 V at 0.1 C.

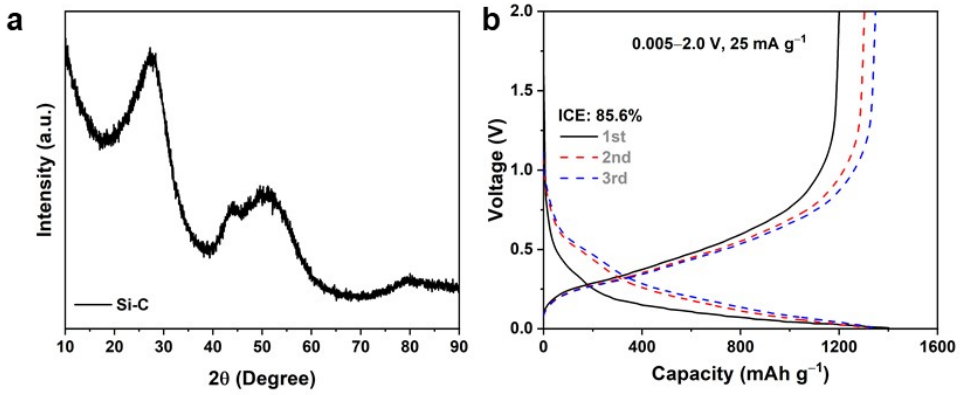

Fig. S28 XRD spectrum of the Si-C anode. (b) Charging-discharging curves of Si-C anode at the current density of 25 mA g^{-1}. The commercial Si-C material has an amorphous structure and a normal discharge specific capacity of 1400 mAh g^{-1}.

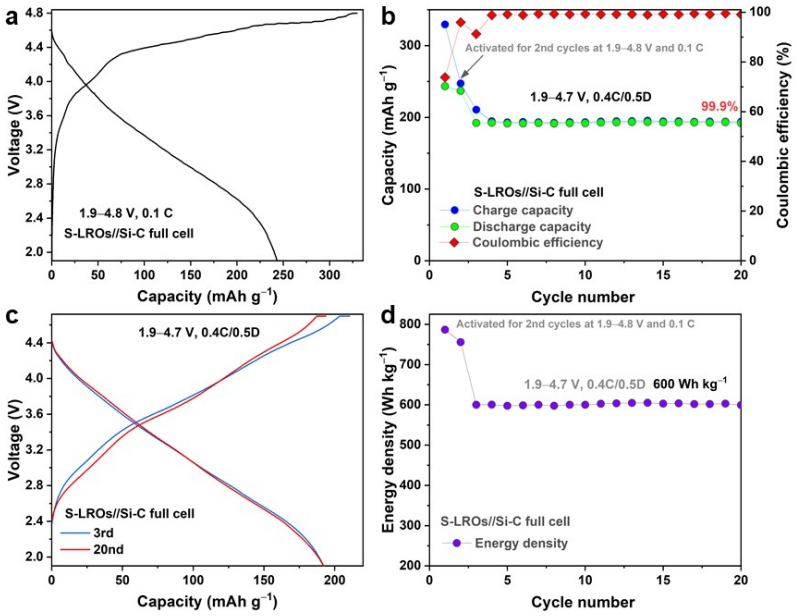

Fig. S29 Electrochemical performance of S-LROs//Si-C full cells. (a) Initial charge/discharge curves in the voltage range of 1.9–4.8 V at 0.1 C. Cycling performance (b) and energy density (d) within the voltage range of 1.9–4.7 V at 0.5 C (0.4 C charge followed by 0.5 C discharge). (c) Charge-discharge curves for the 3rd and 20th. The S-LROs//Si-C cell exhibits a specific capacity of 243.3 mAh g^{-1} with an initial Coulomb efficiency 73.8%. Excitingly, the full battery has negligible capacity degradation after 20 cycles and delivers a high energy density of 600 Wh kg^{-1}.

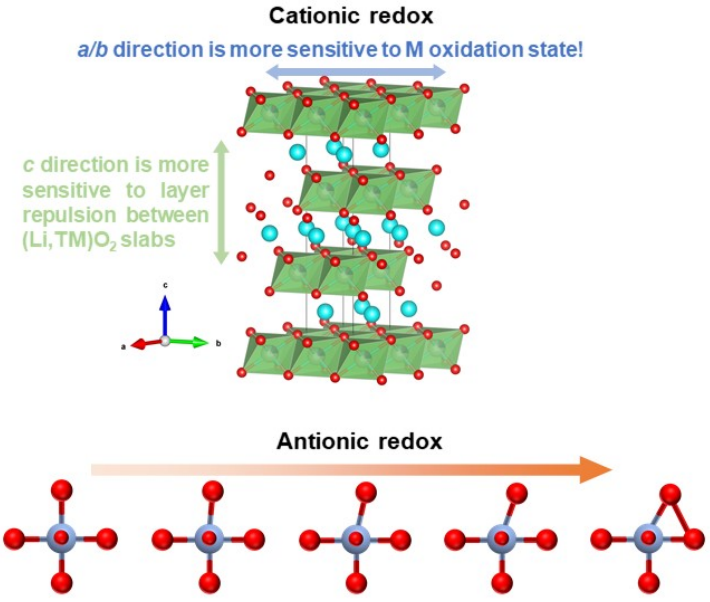

Fig. S30 Schematic diagram of the structural changes during cationic and anionic redox processes.

The lattice parameters in the layered structure show different changes along the *c* and *a* direction. For *a*/*b* direction, the lattice parameters are more sensitive to bond lengths related to the electronic structure of transition metal ions. However, for lattice parameter *c*, it is more sensitive to electrostatic repulsion between the TMO_2 slabs of each other, especially when the Li^+ ions are delithiumized from the Li slabs. As shown in the Fig. 30 (below), local structural distortion occurs during the anionic redox process, while the overall bond length does not change, which is also a key factor in the slow kinetics of the anionic redox process.

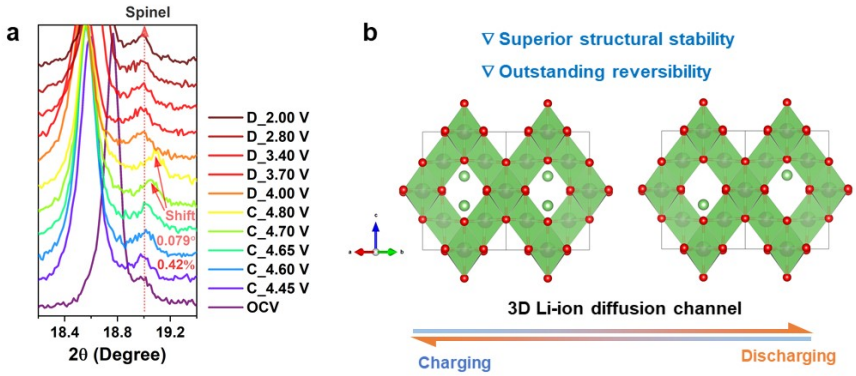

Fig. S31 (a) The XRD spectra corresponding to a specific voltage were selected from the in-situ XRD data of S-LROs, and the diffraction angle ranged from 18.2~19.3°. It is worth noting that during the charging process, the (111) peak of the *in-situ* epitaxial spinel phase ($Li_4Mn_5O_{12}$, $Fd\bar{3}m$) is slightly offset to the high angle (0.079°) above 4.70 V, and the offset is only a negligible 0.42%, especially when discharged, it quickly returns to the original angle and remains unchanged. (b) The schematic diagram of the phase structure characteristics of the spinel phase with a 3D Li^+ ion diffusion path and superior structural stability during charging and discharging.

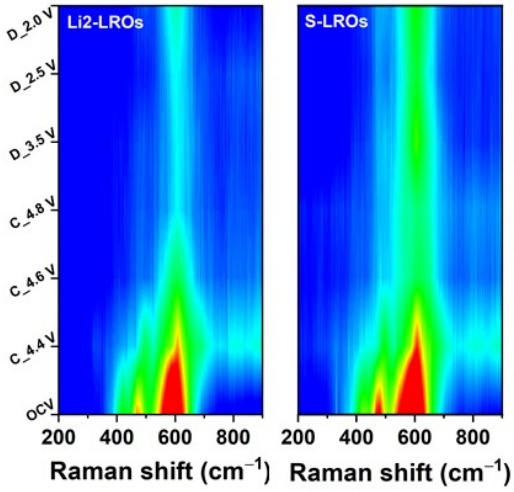

Fig. S32 The *ex-situ* Raman spectra of Li2-LROs and S-LROs during the first charging/discharging process at 0.1 C.

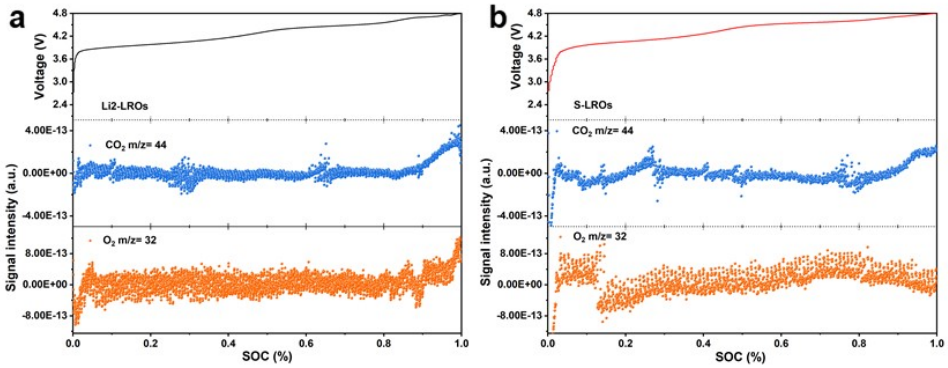

Fig. S33 *Online* DEMS tests in charging of Li2-LROs and S-LROs at 0.2 C.

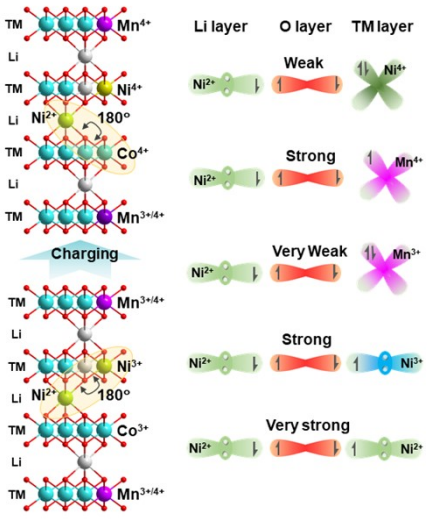

Fig. S34 Schematic of the superexchange interaction between $Ni_{Li\ site}$ and $TM_{TM\ site}$ within LROs at pristine and charging states.

During the synthesis of cathode materials, some Ni^{2+} ions in the metal layer inevitably migrate toward the Li slabs, resulting in a certain content of Li/Ni mixing. As a result, three types of magnetic interactions including linear Ni^{2+}–O^{2-}–Ni^{2+} antiferromagnetic superexchange interactions mediated by oxygen atoms, linear Ni^{2+}–O^{2-}–Mn^{4+} ferromagnetic interactions, as well as the observation of 90° Ni^{2+}–O^{2-}–Mn^{4+} interlayer junctions were observed.

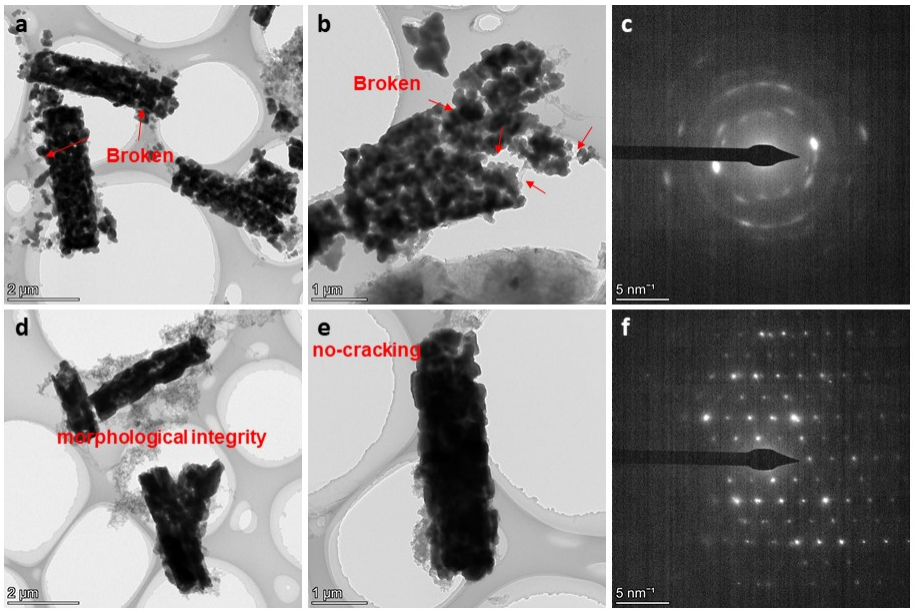

Fig. S35 (a, b) TEM images and (c) selected area electron diffraction (SAED) of the Li2-LROs electrode after 400 cycles. (d, e) TEM and (f) SAED of the S-LROs electrode after 500 cycles.

The stress-strain aggregation on the particle surface during cycling is caused by the lattice anisotropic distortion, and the S-LROs particles are more compact compared to the loose stacking of the secondary particles of the Li2-LROs material, as displayed in Fig. S35a, b and d, e. In addition, as enumerated in Fig. S35c, g, the S-LROs remain well crystallized and layered as observed from the SAED. In contrast, Li2-LROs are poorly crystallized and have phase transitions so severe that no layered structure features can be observed.

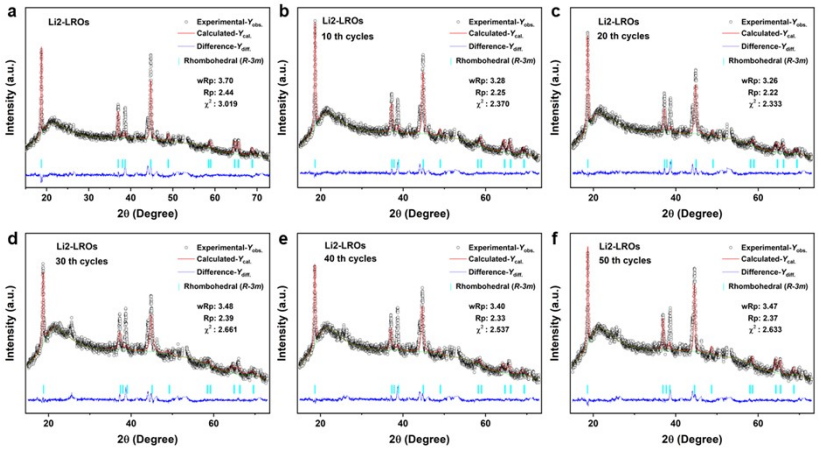

Fig. S36 Refinement results for selected XRD data based on hexagonal ($R\bar{3}m$) phases of Li2-LROs cathodes. Reasonable wRp, Rp and χ^2 fitting parameters ensure the confidence of the refinement results.

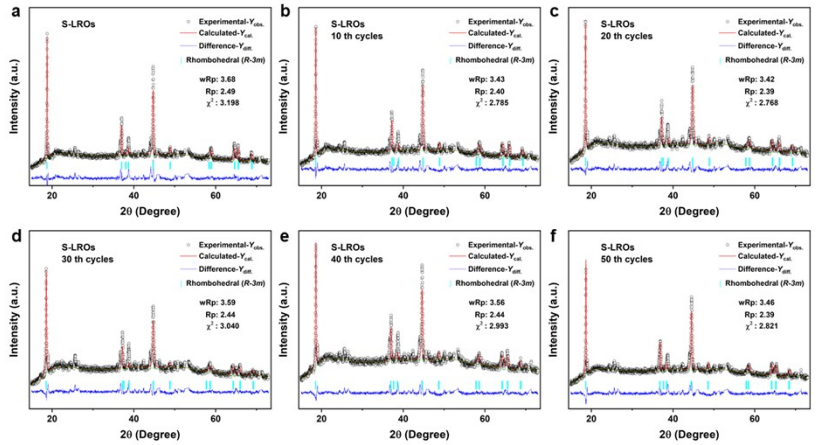

Fig. S37 Refinement results for selected XRD data based on hexagonal ($R\bar{3}m$) phases of S-LROs cathodes. Reasonable wRp, Rp and χ^2 fitting parameters ensure the confidence of the refinement results.

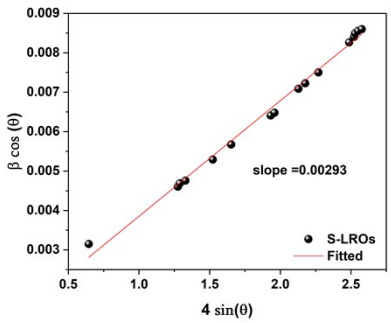

Fig. S38 Williamson-Hall plots of the prepared S-LROs samples.

The Williamson-Hall analysis is based on the following equation:
$\beta_{hkl}\cos\theta = (k\lambda/D) + 4\varepsilon\sin\theta$

where β_{hkl} is the broadening of the diffraction peak measured at full-width at half-maximum (in radians) in the set of (hkl) planes, θ is the Bragg diffraction angle, k is the shape factor ($k = 0.9$), λ is the wavelength of the X-rays, D is the volume weighted crystallite size and ε is the lattice strain.

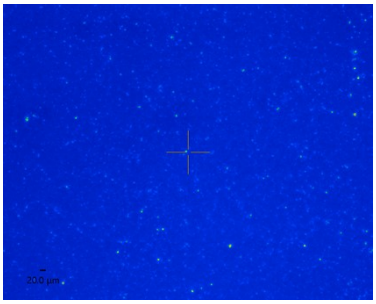

Fig. S39 Optical photograph of an indentation test. The bright areas in the image were selected for indentation testing.

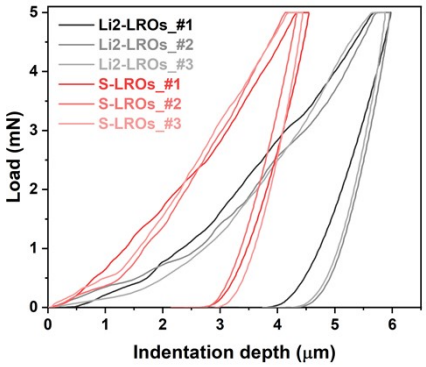

Fig. S40 Load-depth curves of fresh Li2-LROs and S-LROs electrode.

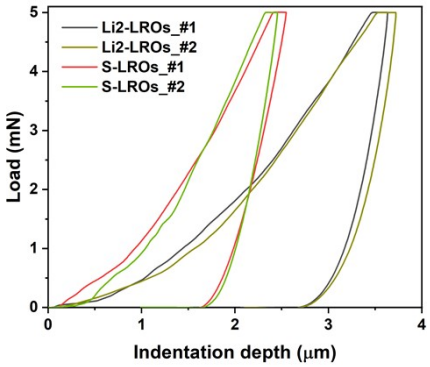

Fig. S41 Load-depth curves of Li2-LROs and S-LROs electrode after 50 cycles at 1 C. The depth of the indentation of the cycled electrodes was less than that of the fresh electrodes, attributed to the fact that the electrodes that were disassembled after assembling the cell were compacted.

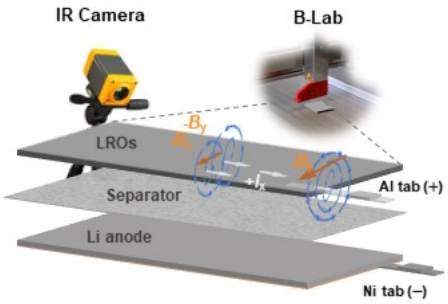

Fig. S42 *Operando* MFI analysis and internal structure schematic of a single-layer pouch cell.

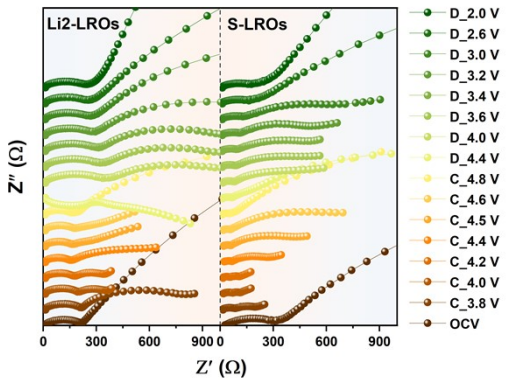

Fig. S43 Comparison of *In-situ* EIS curves of Li2-LROs (left) and S-LROs (right) sample.

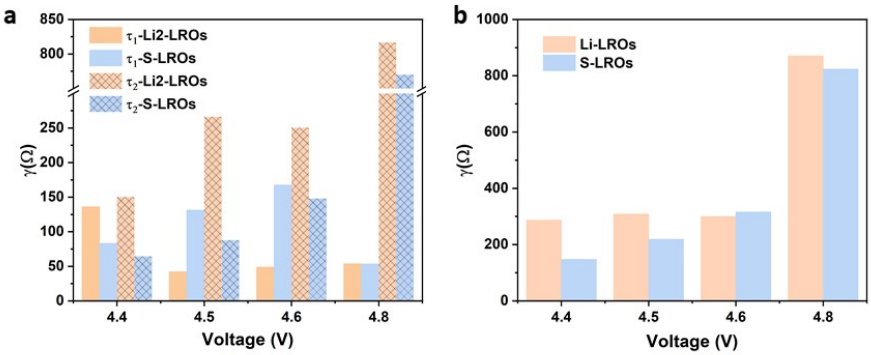

Fig. S44 (a) The integral area obtained by fitting the corresponding time constants τ_1 and τ_2 in Fig. 6b. (b) The sum of the corresponding τ_1 and τ_2 integral areas.

Table S2. Details in strategies and electrochemical performance of LROs in the references

Strategies	**Rate (mA g^{-1}, 2.0~4.8 V)**	**Cycle number**	**Voltage drop per cycle (mV)**	**Capacity retention (%)**	**Ref.**
Entropy-assisted surface engineering	250 (2.0~4.6V)	250	1.6848	88.09	Ref.[S9]
Grain boundaries infusing $LiAlO_2$ material	250	300	1.33	81.84	Ref.[S10]
Oxygen covalent electron localization	250 (2.0~4.65V)	200	1.35	93.6	Ref.[S11]
Surface defects	125	100	2.3	94.5	Ref.[S12]
Modulating the surface ligand orientation	250	300	1.86	85.9	Ref.[S13]
Single-crystal, Double-layer interface engineering	250	300	2.3	81.4	Ref.[S14]
Oxygen-centred structural arrangement	200 (2.0~4.6V)	100	3.17	93.3	Ref.[S15]
Constructing integrated surface structures	250	400	7.3	73.4	Ref.[S16]
Sb-pinning transition metal layers	250	200	6.758	86.03	Ref.[S17]
Surface heterophase coating	250	100	2.99	85.49	Ref.[S18]
Multi-scale defect design	250	320	1.0	96.3	This work
		400	1.08	90.8	
		500	1.15	81.0	

Table S3. Comparison of capacity retention of S-LROs in this work with other spinel phase modified Li-rich oxide cathodes reported previously.

Strategies	**Rate (1C= 250 mA g^{-1}, 2.0~4.8 V)**	**Cycle number**	**Capacity retention (%)**	**Ref.**
Niobium modification	1 C	200 600	78.8 54.8	Ref.[13]
Tuning the Li content ($Li_xMn_{0.54}Ni_{0.13}Co_{0.13}O_2$ samples (x =1.08, 1.14, 1.20, 1.26, denoted as Li-1.08, Li-1.14, Li-1.20 and Li-1.26, respectively)	1 C	100	62.4 in Li-1.26 97.6 in Li-1.20 76.2 in Li-1.14 82.1 in Li-1.08	Ref.[24]
Erucic acid-assisted interface engineering	1 C	200	91	Ref.[44]
Oleic acid-assisted interface engineering	1 C	200	84.1	Ref.[31]
Sulfurization strategy	1 C	100	92.1	Ref.[S19]
Li^+/H^+ exchange	1 C	400	90.7	Ref.[S20]
V-doped	1 C	200	91.9	Ref.[S21]
Multi-scale defect design	1 C	320 400 500	96.3 90.8 81.0	This work

Table S4. Details in strategies, initial coulombic efficiency, voltage drop, and capacity retention are compared with those of marvelous LRO cathodes reported in the last three years.

Strategies	Year	Initial coulombic efficiency (0.1 C)	Rate (1C=250 mA g^{-1}, 2.0~4.8 V)	Cycle number	Voltage drop per cycle (mV)	Capacity retention (%)	Ref.
Single-crystal	2023	82.4	0.3 C	100	2.28	90.6	Ref.[S22]
Coulombic repulsive interactions strategy	2022	Mot mentioned	1 C	250	1	90	Ref.[S23]
Regulating superstructure domain dispersion	2024	79.7	C/3 (2.0~4.5 V)	50	4.5	87.1	Ref.[S24]
Mesostructural design	2022	79.4	0.1 C	120	Mot mentioned	84	Ref.[S25]
Twin structures	2023	Mot mentioned	1 C	200	2.17	85	Ref.[S26]
Strong Nb_{4d}-O_{2p}-Li_{2s} configurations	2024	85	1 C	300	Mot mentioned	81	Ref.[S27]
Multi-scale defect design	––	87.1	1 C	320	1.0	96.3	This work
				400	1.08	90.8	
				500	1.15	81.0	

Table S5. Summary of modulus (E) and hardness (H) strength test results of Li2-LROs and S-LROs electrode after 50 cycles at 1 C

Sample / Trials	S-LROs				Li2-LROs			
	E (GPa)	H (MPa)	h_f (μm)	h_{max} (μm)	E (GPa)	H (MPa)	h_f (μm)	h_{max} (μm)
#1	0.730	44.077	2.004	2.555	0.709	17.853	3.279	3.640
#2	0.989	43.373	2.056	2.460	0.709	16.867	3.378	3.730
Average	0.860	43.725	2.030	2.508	0.709	17.360	3.329	3.685

Table S6. Summary of modulus (E) and hardness (H) strength test results of fresh S-LRO and Li2-LRO electrode

Sample / Trials	S-LROs		Li2-LROs	
	E (GPa)	H (MPa)	E (GPa)	H (MPa)
#1	0.229	14.368	0.141	8.048
#2	0.254	15.865	0.207	7.143
#3	0.293	13.918	0.222	7.272
Average	0.259	14.717	0.190	7.488

Reference in supporting information

1. J. Liu, F. Li, L. Xi, Z. Sun, Y. Yang, J. Shen, S. Yao, J. Zhao, M. Zhu and J. Liu, *Small*, 2024, **20**, 2305606.
2. F. Li, Z. Liu, J. Shen, X. Xu, L. Zeng, B. Zhang, H. Zhu, Q. Liu, J. Liu and M. Zhu, *J. Mater. Chem. A*, 2021, **9**, 2830-2839.
3. M. J. Hÿtch, E. Snoeck and R. Kilaas, *Ultramicroscopy*, 1998, **74**, 131-146.
4. T. H. Wan, M. Saccoccio, C. Chen and F. Ciucci, *Electrochim. Acta*, 2015, **184**, 483-499.
5. N. Yabuuchi, K. Yoshii, S.-T. Myung, I. Nakai and S. Komaba, *J. Am. Chem. Soc.*, 2011, **133**, 4404-4419.
6. Q. Shao, P. Gao, C. Yan, M. Gao, W. Du, J. Chen, Y. Yang, J. Gan, Z. Wu, C. Zhang, G. Chen, X. Zheng, Y. Lin, Y. Jiang, W. Sun, Y. Liu, M. Gao and H. Pan, *Adv. Mater.*, 2022, **34**, 2108543.
7. A. Gao, Q. Zhang, X. Li, T. Shang, Z. Tang, X. Lu, Y. Luo, J. Ding, W. H. Kan, H. Chen, W. Yin, X. Wang, D. Xiao, D. Su, H. Li, X. Rong, X. Yu, Q. Yu, F. Meng, C. Nan, C. Delmas, L. Chen, Y.-S. Hu and L. Gu, *Nat. Sustain.*, 2022, **5**, 214-224.
8. S. D. Kang and W. C. Chueh, *J. Electrochem. Soc.*, 2021, **168**, 120504.
9. J. Zhao, Y. Su, J. Dong, Q. Shi, Y. Lu, N. Li, H. Wang, Y. Fang, W. Li, J. Hao, Y. Wu, Q. Qi, F. Wu and L. Chen, *Energy Storage Mater.*, 2024, **70**, 103550.
10. W. He, C. Zhang, M. Wang, B. Wei, Y. Zhu, J. Wu, C. Liang, L. Chen, P. Wang and W. Wei, *Adv. Funct. Mater.*, 2022, **32**, 2200322.

11. C. Zhang, B. Wei, M. Wang, D. Zhang, T. Uchiyama, C. Liang, L. Chen, Y. Uchimoto, R. Zhang, P. Wang and W. Wei, *Energy Storage Mater.*, 2022, **46**, 512-522.
12. Y. Pei, Q. Chen, M. Wang, B. Li, P. Wang, G. Henkelman, L. Zhen, G. Cao and C.-Y. Xu, *Nano Energy*, 2020, **71**, 104644.
13. Y. Liu, H. Zhu, H. Zhu, Y. Ren, Y. Zhu, Y. Huang, L. Dai, S. Dou, J. Xu, C.-J. Sun, X.-L. Wang, Y. Deng, Q. Yuan, X. Liu, J. Wu, Y. Chen and Q. Liu, *Adv. Energy Mater.*, 2021, **11**, 2003479.
14. W. Zeng, F. Liu, J. Yang, B. Zhang, F. Cao, W. Tian, J. Wang, R. Yu, F. Xia, H. Peng, J. Ma, Z. Wang, S. Mu and J. Wu, *Energy Storage Mater.*, 2023, **54**, 651-660.
15. S. Myeong, W. Cho, W. Jin, J. Hwang, M. Yoon, Y. Yoo, G. Nam, H. Jang, J.-G. Han, N.-S. Choi, M. G. Kim and J. Cho, *Nat. Commun.*, 2018, **9**, 3285.
16. D. Luo, H. Xie, F. Tan, X. Ding, J. Cui, X. Xie, C. Liu and Z. Lin, *Angew. Chem. Int. Ed.*, 2022, **61**, e202203698.
17. F. Cao, W. Zeng, J. Zhu, J. Xiao, Z. Li, M. Li, R. Qin, T. Wang, J. Chen, X. Yi, J. Wang and S. Mu, *Small*, 2022, **18**, 2200713.
18. Y. Su, F. Yuan, L. Chen, Y. Lu, J. Dong, Y. Fang, S. Chen and F. Wu, *J. Energy Chem.*, 2020, **51**, 39-47.
19. Y. Lee, T.-H. Kim, Y.-K. Kwon, J. Shin and E. Cho, *ACS Sustainable Chem. Engin.*, 2020, **8**, 8037-8048.
20. L. Wang, L. Xu, W. Xue, Q. Fang, H. Liu, Y. Liu, K. Zhou, Y. Li, X. Wang, X. Wang, X. Yang, X. Yu and X. Wang, *Nano Energy*, 2024, **121**, 109241.
21. L. Tan, W. Huang, X. Xie, X. Li, Z. Liang, Z. Lin, C. Liu and D. Luo, *Energy Mater. Dev.*, 2024, **2**, 9370039.
22. M. Yoon, Y. Dong, Y. Huang, B. Wang, J. Kim, J.-S. Park, J. Hwang, J. Park, S. J. Kang, J. Cho and J. Li, *Nat. Energy*, 2023, **8**, 482-491.
23. Q. Li, D. Ning, D. Wong, K. An, Y. Tang, D. Zhou, G. Schuck, Z. Chen, N. Zhang and X. Liu, *Nat. Commun.*, 2022, **13**, 1123.
24. G. Choi, U. Chang, J. Lee, K. Park, H. Kwon, H. Lee, Y.-I. Kim, J. H. Seo, Y.-C. Park, I. Park, J. Kim, S. Lee, J. Choi, B. Yu, J.-H. Song, H. Shin, S.-W. Baek, S. K.

Lee, H. Park and K. Jung, *Energy Environ. Sci.*, 2024, **17**, 4634-4645.

25. T. Liu, J. Liu, L. Li, L. Yu, J. Diao, T. Zhou, S. Li, A. Dai, W. Zhao, S. Xu, Y. Ren, L. Wang, T. Wu, R. Qi, Y. Xiao, J. Zheng, W. Cha, R. Harder, I. Robinson, J. Wen, J. Lu, F. Pan and K. Amine, *Nature*, 2022, **606**, 305-312.
26. Y. Yang, C. Gao, T. Luo, J. Song, T. Yang, H. Wang, K. Zhang, Y. Zuo, W. Xiao, Z. Jiang, T. Chen and D. Xia, *Adv. Mater.*, 2023, **35**, 2307138.
27. K. Hu, H. Tang, B. Zheng, L. Yu, F. Xiong, H. Li, L. Qiu, F. Wan, Y. Song, B. Zhong, Z. Wu and X. Guo, *Angew. Chem. Int. Ed.*, 2024, e202413563. DOI: 10.1002/anie.202413563